EUROPEAN ORGANIZATION FOR NUCLEAR RESEARCH

CERN–PPE/XX–XXX
22 May 1997

Performance of the Drift Tubes for the Barrel Muon Chambers of the CMS Detector at LHC

S. Bethke, B. Fehr, H. Reithler, H. Schwarthoff, H. Teykal, J. Vandenhirtz, H. Wagner

III. Physikalisches Institut der RWTH Aachen
Sommerfeldstrasse 26-28, D-52074 Aachen, Germany

A. Benvenuti, V. Giordano, M. Guerzoni, S. Marcellini, A. Montanari, F.L. Navarria, A.M. Rossi, T. Rovelli, V. Tano

I.N.F.N. Sezione di Bologna and Dipartimento di Fisica Università di Bologna
Via Irnerio 46, I-40126 Bologna, Italy

J. Berdugo, M. Cerrada, N. Colino, P. Ladrón de Guevara, J. Mocholí, L. Romero

CIEMAT - Division de Fisica de Particulas
Avenida Complutense 22, E-28040 Madrid, Spain

M. Benettoni, M. De Giorgi, A. De Min, U. Dosselli, C. Fanin, F. Gasparini, R. Giantin, I. Lippi, R. Martinelli, F. Mazzucato, A. Meneguzzo, M. Pegoraro, P. Ronchese, A.J. Ponte Sancho, P. Sartori, P. Zotto, G. Zumerle

I.N.F.N. Sezione di Padova and Dipartimento di Fisica Università di Padova
Via Marzolo 8, I-35131 Padova, Italy

Abstract

The barrel muon chambers of the CMS detector consist of three sets of four layers of rectangular drift tubes. The performance of several prototypes was measured in a muon beam for various experimental conditions. Special emphasis was given to study performance aspects related to the trigger capability of the chambers.

(To be Submitted to Nucl. Inst. and Meth.)

1 Introduction

The barrel muon detector of the CMS experiment [1] must provide muon identification, tracking and triggering, the latter being the most demanding feature required. The detector chosen by the CMS collaboration is based on 4 layers of rectangular drift tubes.

The properties of such detectors have been studied with several prototypes and the results have already been published [2, 3]. Recently the design has been optimised with a choice of a new cell structure, construction material and construction technique, leading to a completely revised version suitable for mass production for the CMS detector.

To verify that the new design met the final specifications required for the CMS experiment, another set of prototypes was constructed and tested in a muon beam at the CERN-SpS.

2 Detector Description

The barrel muon detector of the CMS experiment consists of four concentric measuring stations located inside the iron return yoke of the 4 Tesla field generated by a super-conductive solenoidal magnet.

The barrel is 13.5 m long and is divided into 5 wheels. Each wheel comprises 12 azimuthal sectors giving a total of 240 muon stations. The azimuthal arrangement of the muon stations is illustrated in fig. 1 which shows the transverse view of one of the wheels.

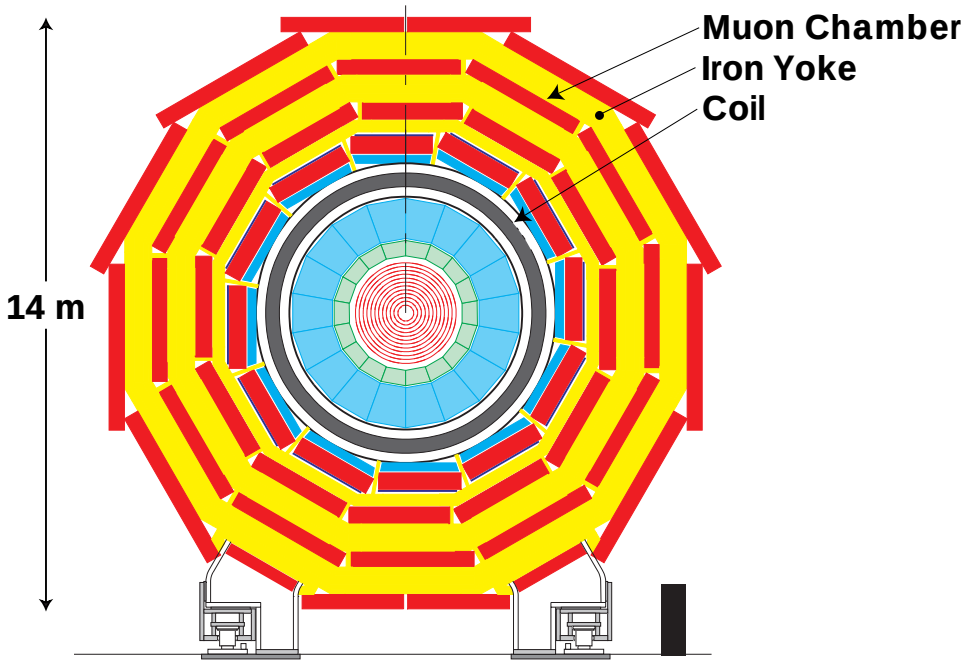

Figure 1: *Transverse view of one wheel of the CMS detector.*

A muon station consists of the drift tube chamber and one or two layers of resistive plate chambers.

Each drift tube chamber (fig. 2) is made of 3 sets of 4 layers of rectangular drift cells (quadruplet) staggered by half a cell. The wires in the two external quadruplets are parallel to the beam line and provide the track measurement in the bending plane. In the internal quadruplet the wires are orthogonal to the beam line and measure the track position along the beam. The chambers are all 29 cm thick and 2.5 m long but have different widths varying from 2 m for the inner stations to 4 m for the outer ones.

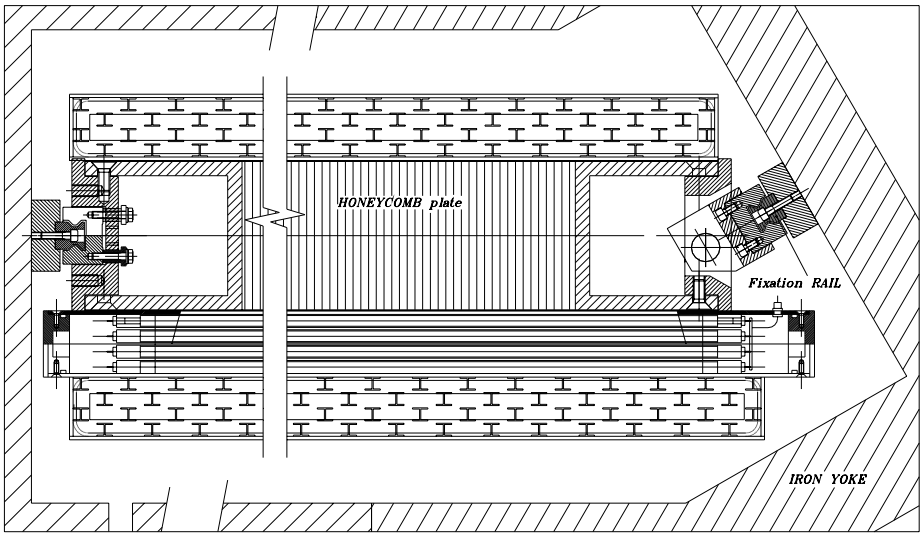

Figure 2: *Transverse view of a Muon Chamber.*

A chamber is assembled by gluing the quadruplets to an aluminium honeycomb plate, as shown in fig. 2. The thickness of the honeycomb, 13 cm, is chosen to provide the required chamber stiffness and also an adequate angular resolution for the muon trigger.

Each quadruplet is made of 5 aluminium sheets, 2 mm thick, separated by 10 mm high aluminium I-beams, 1 mm thick.

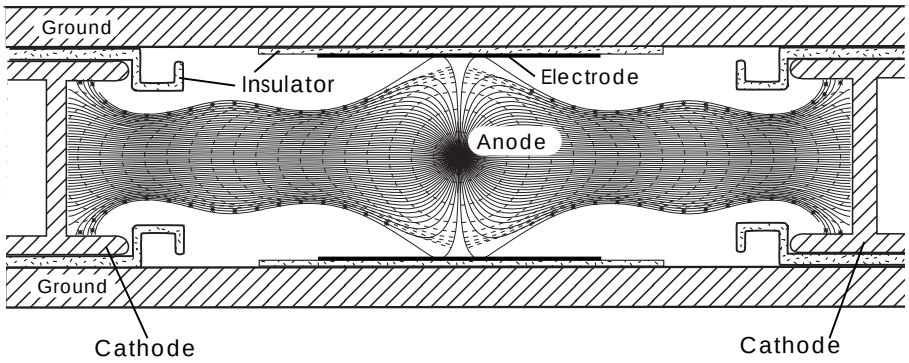

Figure 3: *Transverse view of a Cell.*

The drift cell, shown in fig. 3, has a rectangular section and a pitch of 4.0×1.3 cm^2. The anode is a 50 μm diameter stainless steel wire and the cathodes are the aluminium I-beams which are electrically isolated from the ground planes by polycarbonate (Lexan) strips, 0.5 mm thick. A field shaping electrode, consisting of a 14 mm wide copper strip attached to a 20 mm wide mylar backing, is added above and below the wire to improve the field regularity and strength and hence the linearity of the space-time relation, and to reduce the sensitivity to stray magnetic fields.

A design requirement for the drift tube chambers is to provide track segments with a precision of 100 μm and 1 mrad respectively for position and angular measurements in the bending plane. With the size and structure of the chambers this implies a single cell resolution of 250 μm or better.

For triggering purpose, each muon station must identify the bunch crossing asso-

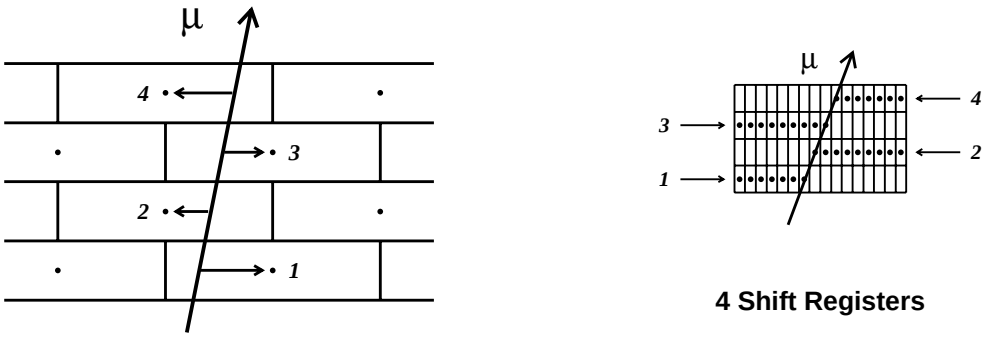

Figure 4: *Schematic representation of the Mean Timer technique used for the trigger.*

ciated with the muon (LHC will have a bunch crossing every 25 ns) and give a coarse measurement of the position and incidence angle to the global trigger processor to apply a momentum cut.

The trigger is generated by each quadruplet with a Mean Timer technique [2], which is made possible by the staggering of the drift cells. As shown in fig. 4, the signal of each wire is injected into a shift register clocked at 80 MHz, i.e. twice the bunch crossing frequency. The alignment of the bits in the four shift registers occurs at a fixed time after the track crossing, equal to the maximum drift time, thus allowing the bunch crossing identification. Moreover, the image formed by the aligned bits in the bit matrix is a *picture* of the crossing track, thus allowing an estimate of its angle and position.

A good linearity, required for the application of the Mean Timer technique, is obtained by maintaining the electric field along the cell at a sufficient strength to guarantee a saturated drift velocity. The drift velocity for the gas mixture used, Ar(85%) and CO_2(15%), and the drift field on the median plane of the cell were simulated using the program GARFIELD [4] and are shown in fig. 5.

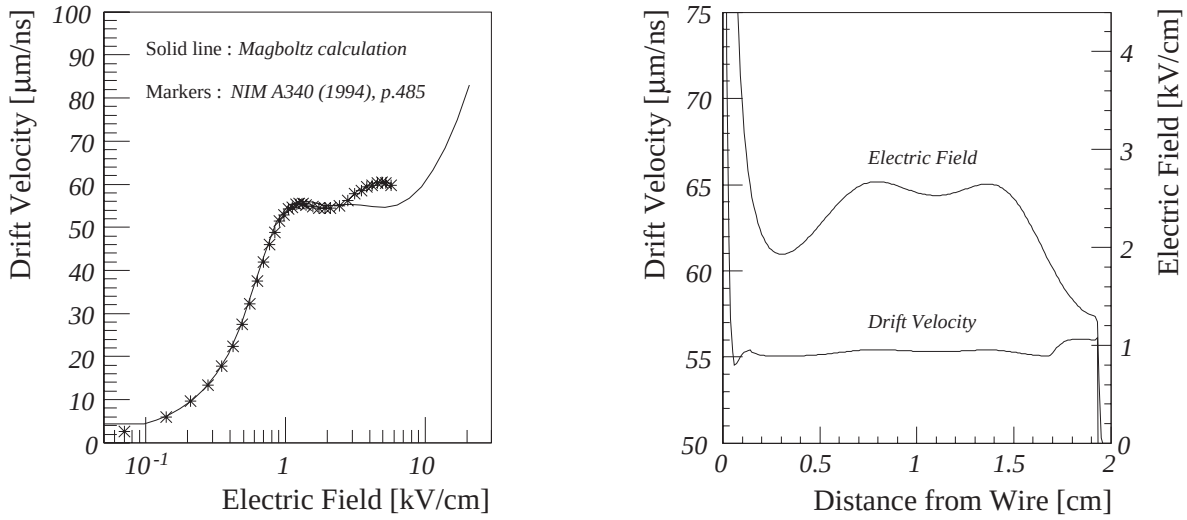

Figure 5: a) *Drift velocity for the Ar(85%) and CO_2(15%) gas mixture as calculated (solid line) and measured (markers).* b) *Calculated electric field along the drift space for reference voltages settings and corresponding drift velocity.*

3 Experimental Setup

Several prototypes, reduced size versions of the quadruplet, were exposed to muon beams with 200-300 GeV energy in the H2 test beam area at the CERN-SpS, during August 1995 and in the period April to July 1996.

The Q1 prototype, built in Padova by the Bologna and Padova groups, is 1 m long and 16 cells wide, for a total of 64 drift tubes. It was equipped with the ASD-8 amplifier-shaper-discriminator chip [5], capacitively coupled to the anode wires. The output signal was then stretched to a width of 80 ns and buffered in ECL levels to drive the long twisted pair cables by a dedicated circuit.

The quadruplet prototype built in Aachen consists of 32 drift tubes with 1 m long wires. To compare directly the influence of the electric field shaping on the drift time resolution under various experimental conditions, half of the drift cells were not equipped with central electrodes. The analog signals of the Aachen prototype were fed into preamplifiers, attached directly to the anode wires via HV-capacitors. The amplified signals were discriminated on the chamber body and driven as 50 ns long ECL pulses.

Data were also taken in 19 96 with a third prototype built at CIEMAT-Madrid having four quadruplets, 48 drift tubes each, 50 cm long. Two of the quadruplets had vertical wires and the other two horizontal wires, thus simulating the configuration of the CMS barrel muon stations. Preamplifiers and discriminator cards from the L3 experiment were used [6], the preamplifiers being placed about 30 to 40 cm away from the wire ends.

A wide range of discriminating thresholds was covered during data taking, the reference value being equivalent to 4 fC.

The drift times were digitised with 1 ns resolution by the 32-channel, multi-hit, LeCroy-2277 TDC, using the *common stop* mode.

The chambers were operated with a Ar(85%) CO_2(15%) gas mixture at different voltages, the reference settings being :

- $V_{wire} = 3600\,V$
- $V_{strip} = 1800\,V$
- $V_{cathode} = -1800\,V$.

Since it was always kept $V_{strip} = -V_{cathode}$, the working point will be identified by the following notation :

- $V_{ampl} = V_{wire} - V_{strip}$
- $V_{drift} = V_{strip} - V_{cathode}$.

To study the performance of the chamber as a function of the muon impact angle the chambers were mounted on a special fixture which allowed to rotate it around an axis parallel (*transverse* incidence angle) or orthogonal (*longitudinal* incidence angle) to the wires.

During the June 1996 data taking period a prototype custom chip (MAD) developed in Padova was tested in place of the ASD-8. The integrated circuit contains 2 independent channels made of a charge preamplifier followed by a fast discriminator and a pulse stretcher, the output being able to drive long twisted pair cables.

Unless otherwise stated, the voltages and threshold settings were at the reference values and the electronics used was the ASD-8 chip.

4 Noise

Two different types of noise which could affect the track identification and trigger capability of the chambers were considered : random and correlated noise. They generate extra hits causing wrong track associations and spurious triggers.

4.1 Random Noise

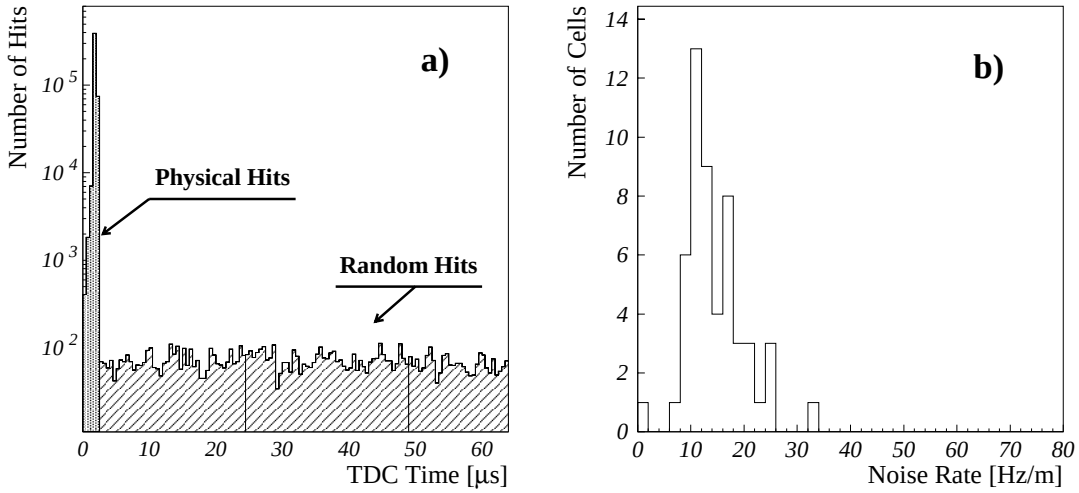

Figure 6: *Distribution of* a) *all the times as recorded by the TDC's and* b) *the random noise of each cell in Hertz per meter.*

The random noise generated by the cells was measured using the TDC multi-hit capability and its full 64 μs active time range. Particles crossing the chamber give hits within a restricted TDC time range, i.e. < 2.1 μs, while noise hits are distributed across the whole TDC range, see fig. 6a. The random noise rate can be calculated by counting the number of hits recorded outside the restricted time range in each cell. With the chamber operating at the reference settings the random noise rate per cell was found to be in the range 10 to 20 Hz/m, (fig. 6b).

At LHC the physical hit rate is expected to be of the order of 1 kHz per channel. With this rate the probability of a random hit to occur within the drift time of a physical hit, 350 ns, and thus to be a nuisance to the pattern recognition and track reconstruction, is below 2%.

4.2 Correlated Noise

Hits generated after a physical hit on a cell are ascribed to correlated noise. These signals can be generated by a genuine late arrival of an electron cluster produced by the ionization process inside the cell, or by the electronic processing of the physical signals. In the first case the noise rate is irreducible while in the second case it can be reduced through the optimisation of the electronics.

The rate of correlated noise produced in a cell can be measured by counting the number of multiple hits produced after the passage of a particle in that cell. As is shown in Fig. 7a, about 12% of the hits are accompanied by one extra hit and 2% by more than one hit.

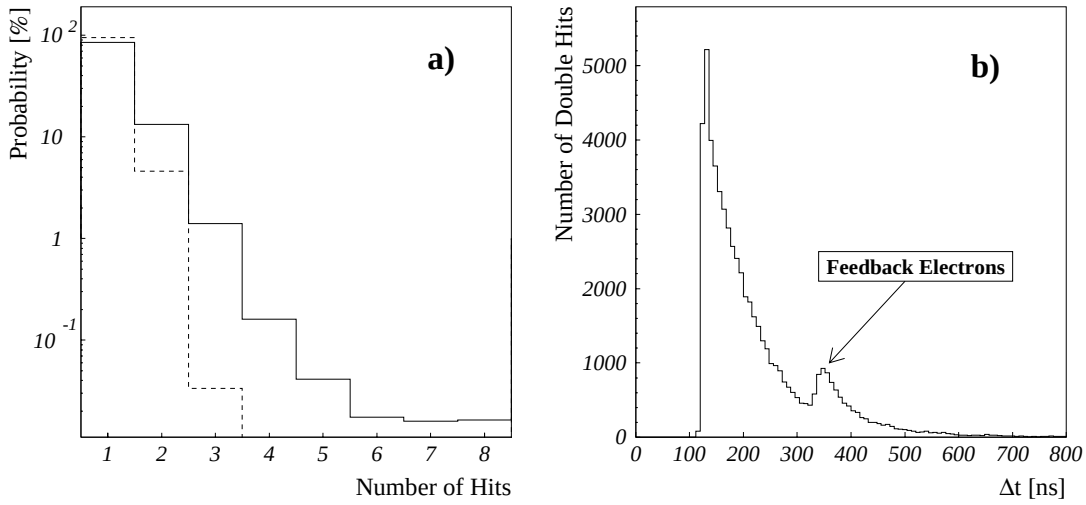

Figure 7: a) *Hit multiplicity, in percent, for a single cell with the ASD-8 chip (full line) and the new electronics (dashed line).* b) *Distribution of the time difference between the first and the second hit for cells with two hits.*

As the comparison between the different types of electronics shows, a substantial fraction of multiple hits can be in large part attributed to a poor coupling of the electronics to the ASD-8 chip. When the ASD-8 was replaced with the MAD chip the single extra hit rate dropped to 5% and the rate for more than one hit became negligible. Furthermore a double hit rate comparable to the one obtained with the MAD was measured with the Aachen prototype.

4.2.1 Correlated Noise : Feedback Electrons

A special case of correlated noise are the *feedback electrons*. The photons produced during the multiplication process can extract from the cathode electrons which drift back to the anode wire. The resulting signals are correlated in time with the physical hits and are produced at a fixed delay time, equal to the maximum drift time.

The high gain voltage, the low quenching power of the gas mixture and the bulk of metal material in the cell structure impose a careful evaluation of the production rate of the feedback electrons.

The presence of feedback electrons is clearly visible in the distribution of the time difference for double hit events shown, in fig. 7b, as an excess of events over the exponential distribution starting at the maximal drift time.

The probability for a feedback electron pulse to occur after a physical hit is estimated to be well below 1% at the reference settings.

4.3 Cross-Talk

Hits produced by a physical signal in nearby channels due to electric coupling are usually referred to as cross-talk.

The contribution of cross-talk to the overall noise was estimated from the time difference of each track hit with any other hit in the surrounding cells. The cross-talk hits are expected to occur at about the same time as the physical hit.

The resulting distribution, shown in fig. 8, has a clear peak around zero over a background due mainly to electromagnetic secondaries accompanying the muon. This background is uncorrelated in time and was estimated by taking the time difference of hits generated in different events.

Another peak is also visible about 120 ns later, which is the intrinsic dead time of the electronics coupled to the ASD-8 chip. This contribution is attributed to the inappropriate coupling of the two components of the electronic chain.

The amount of cross-talk was evaluated from fig. 8, calculating the excess of entries with respect to the background, normalised to the negative part of the spectrum, which is not biased by the peaks themselves. Taking only the excess of events around zero we find that less than 0.5% of the crossing tracks generate a nearly synchronous spurious hit in a surrounding cell.

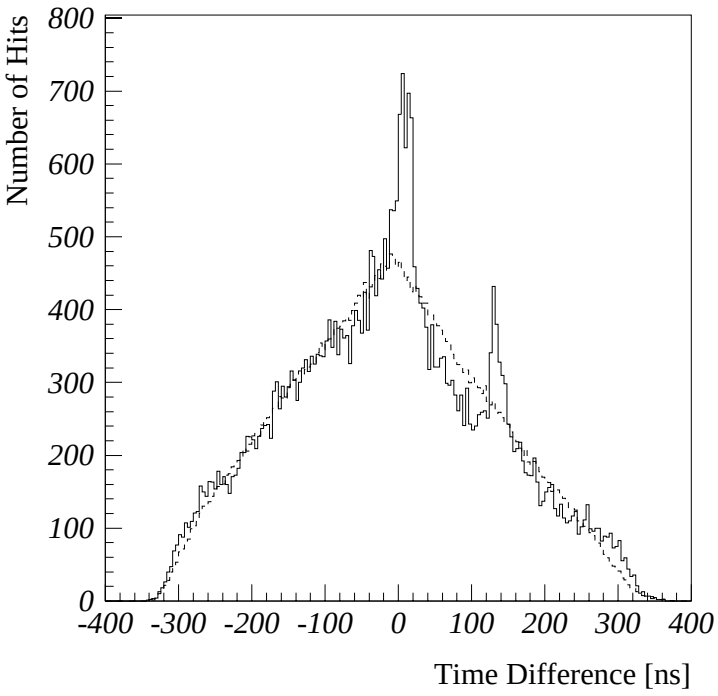

Figure 8: *Distribution of the time difference between a track hit and a hit in the surrounding cells. The dashed line represents the normalised combinatorial background.*

5 Efficiency

The efficiency was measured for each half-cell, using data taken with the beam orthogonally incident.

A sample of clean events was selected by requiring one hit per plane, excluding the plane under study, and that the three hits fit a straight line with residuals less than 2.5 standard deviations. The position of the track inside the half-cell was computed in 1 mm bins by interpolation or extrapolation of the fitted trajectory. The efficiency was calculated for each bin by requiring a hit in the half-cell within the physical drift time. The half-cell efficiency was obtained averaging over all bins.

This procedure allows to evaluate the intrinsic cell efficiency, i.e. inside the geometrical acceptance, and to avoid systematic effects due to possible non-uniformities inside the cell.

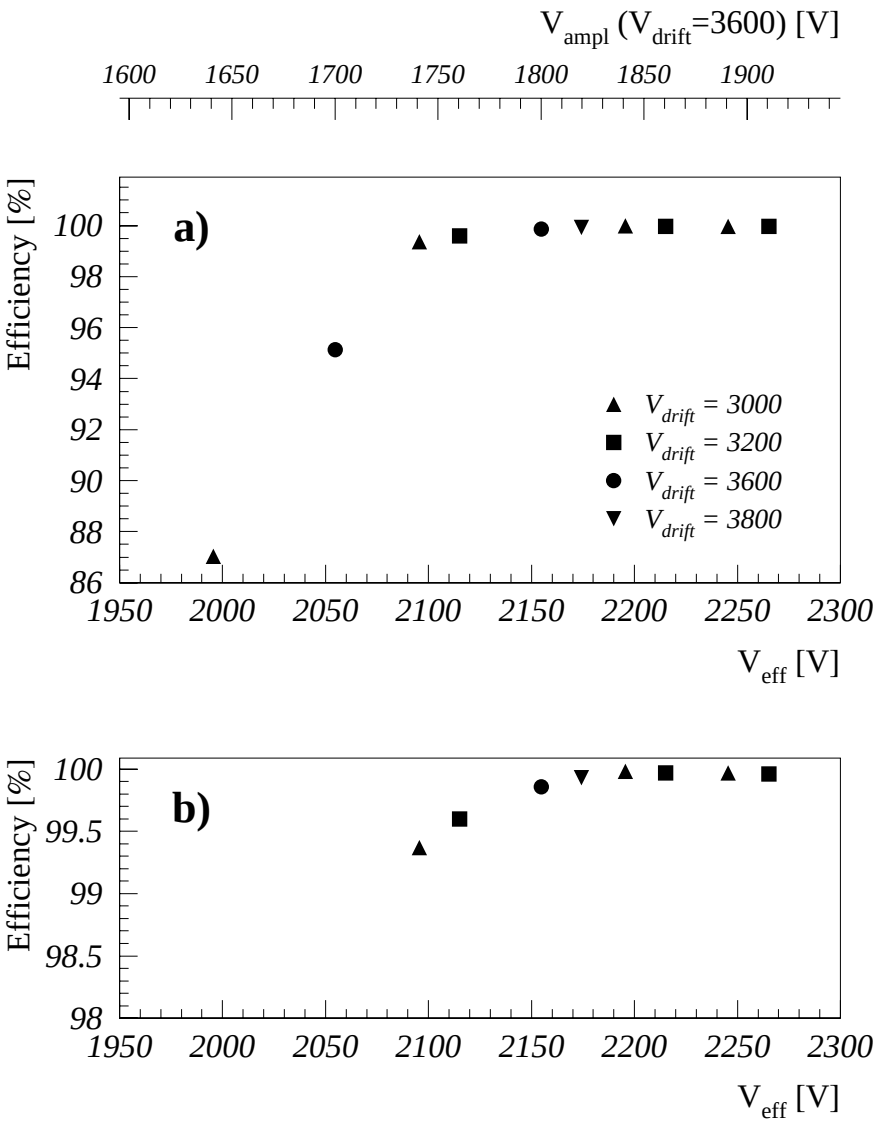

Figure 9: *Intrinsic cell efficiency as a function of the effective voltage* V_{eff}*, proportional to the electric field on the wire* (a)*; with an expanded scale* (b).

In fig. 9, the average cell efficiency obtained at different voltage settings is given as a function of the effective voltage V_{eff}, which is a quantity proportional to the electric field on the wire.

V_{eff} is related to the gas amplification M by the relation

$$M \;=\; A\, e^{\alpha V_{eff}} \tag{1}$$

and can be parametrised as a function of the voltage settings (in Volts) by the following relation :

$$V_{eff} \;=\; (\, V_{wire} \;-\; V_{strip}\,) \;+\; 0.16\, V_{strip} \;-\; 0.037\, V_{cathode} \tag{2}$$

The parameters were determined experimentally through an extensive study of the gas amplification with a radioactive source [7].

Efficiency measurements made at different voltage settings lie on the same curve, indicating that the gas amplification is the significant parameter affecting the value of the efficiency.

The inefficiency is very low, 0.2%, when the chamber is operated at the reference voltages : $V_{ampl} = 1800$ V and $V_{drift} = 3600$ V. It is nevertheless important to verify that such inefficiency is not concentrated in particular regions of the cell, where it might be much larger. A plot of the inefficiency as a function of the position of the track in the cell, shown in fig. 10, gives evidence for such a behaviour : the small efficiency drop occurs in correspondence of the edges of the Lexan strips which isolate the I-beams from the ground plane (fig. 3).

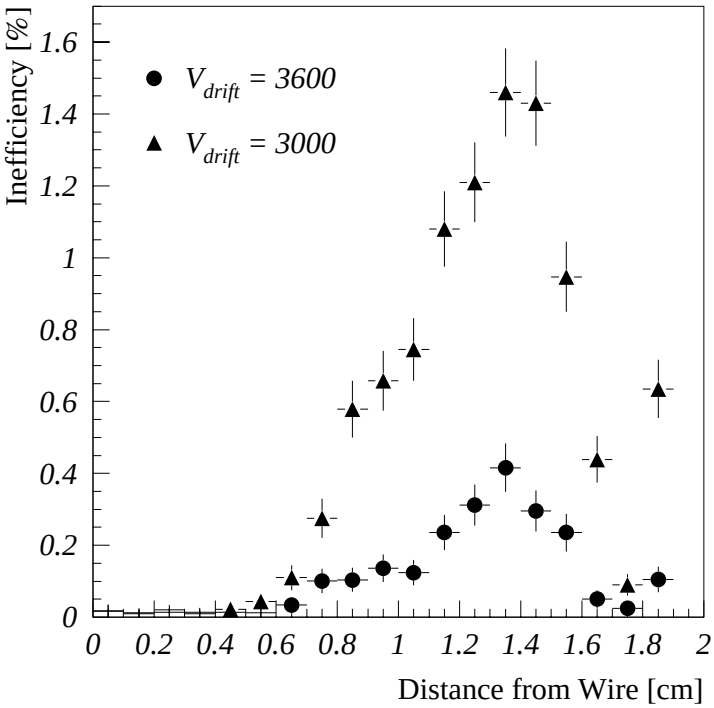

Figure 10: *Cell inefficiency as a function of the track crossing position for two voltage settings, both with* $V_{drift} = 3000$ V.

This small inefficiency could be attributed to the distortions of the drift lines caused by the presence of a dielectric, resulting in a shorter effective track length for the production of the ionization clusters. Such effect is confirmed by the plots in fig. 11, where the efficiency is shown for different values of the transverse incidence angle. The small inefficiency disappears as the angle of incidence makes the available track length longer. The same behaviour is observed for longitudinal incidence angles. Given the wide range of impact angles expected in CMS the effects of such inefficiency are completely negligible.

The last point of the plot in fig. 10, corresponding to a 1 mm region, is strongly affected by the geometrical acceptance due to the presence of the I-beam, resulting in an inefficiency out of the plot scale. It was not included in the total cell efficiency calculations.

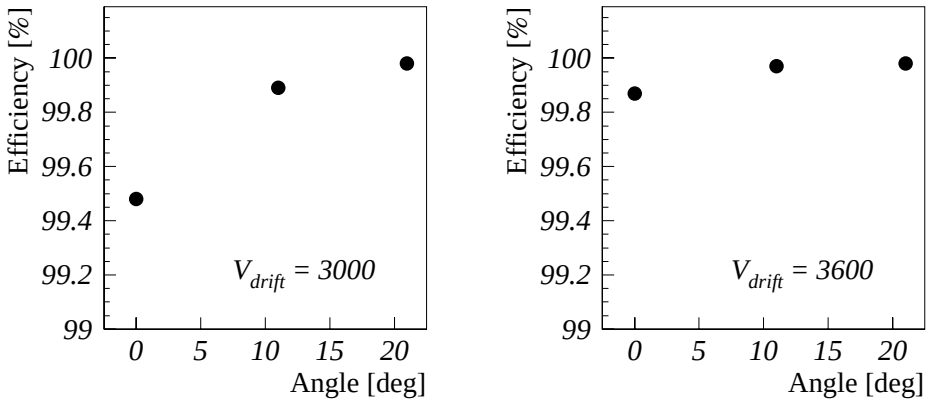

Figure 11: *Cell efficiency for different incidence angles on the plane transverse to the wires, and two voltage settings.*

The dependence of the efficiency on the threshold applied to the signal was studied with the Q1 prototype and the ASD-8 electronics. No significant drop of the efficiency was observed varying the threshold from 1 to 6 fC.

Data were also collected with the CIEMAT-Madrid prototype and the respective electronics with a wider range of discriminator thresholds and with $V_{drift} = 3000$ V. The results, shown in fig. 12, indicate that a significant efficiency loss occurs for thresholds larger than 8 fC.

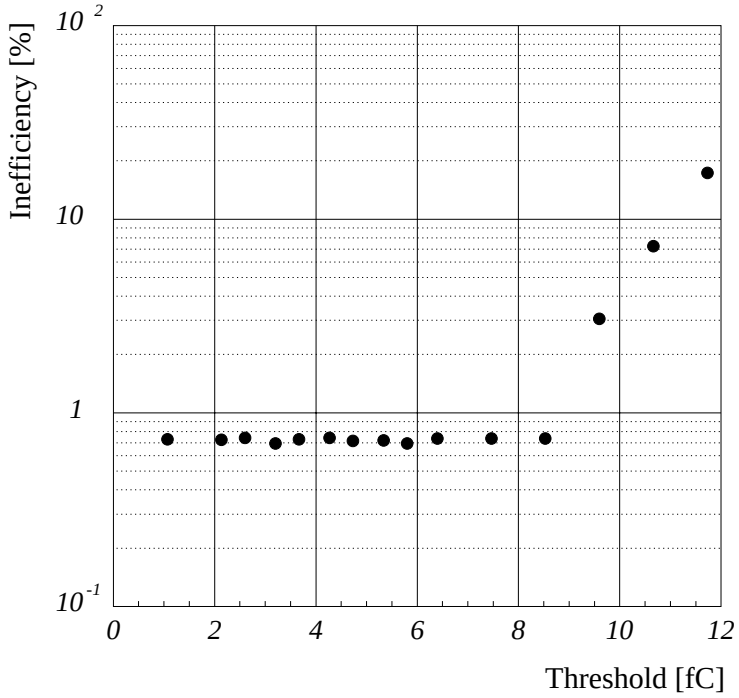

Figure 12: *Cell efficiency for different discriminator thresholds with the CIEMAT-Madrid prototype at* $\mathrm{V_{drift}} = 3000\,\mathrm{V}$ *and* $\mathrm{V_{ampl}} = 1800\,\mathrm{V}$ *and the respective electronics.*

6 Trigger Efficiency

The trigger of a quadruplet is given by the alignment of three hits out of four, as described in sect. 2. The electromagnetic interactions of the crossing muon with the chamber gas and material can generate parasitic tracks which constitute a significant source of inefficiency, as they strongly affect the track measurement and triggering by spoiling the correlation between the drift time and the track position. This is shown schematically in fig. 13a for the drift time t_3.

The influence of the electromagnetic interactions of the crossing muons on the trigger efficiency has already been studied with the previous prototypes and the results have been reported in [3]. The bulk of metal material of the present version of the chamber imposes a renewal of the analysis.

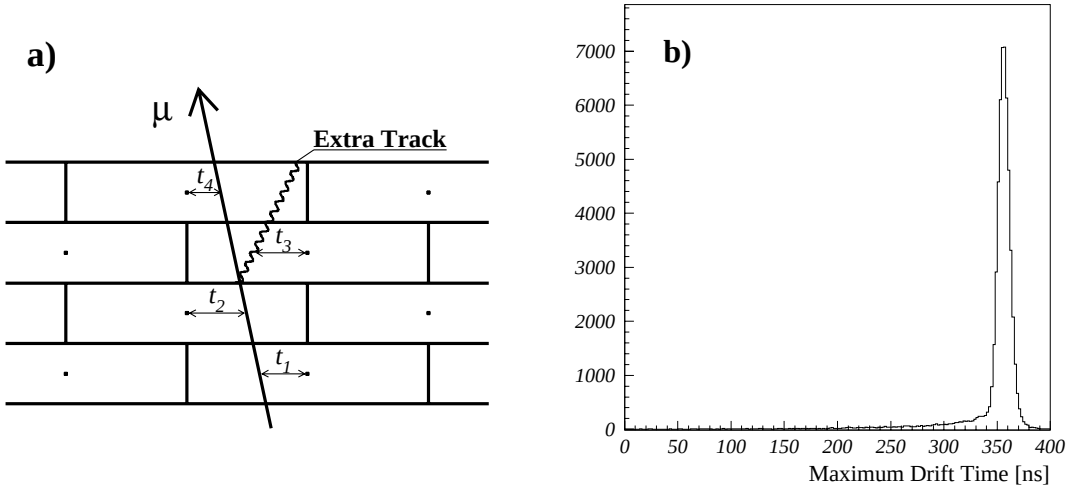

Figure 13: a) *A parasitic track, produced by a crossing μ, affects the drift time t_3.* b) *Maximum drift time defined as* $(t_1 + t_3)/2 + t_2$.

The effects of parasitic tracks production on the drift time measurements was evaluated using the variables MT_2 and MT_3, defined as :

$$MT_j = (t_{j-1} + t_{j+1})/2 + t_j \tag{3}$$

calculated from a sample of orthogonally incident tracks. These quantities should have a constant value, equal to the maximum drift time, independently of the angles of the incident particles.

Fig. 13b shows the distribution of the mean time of three consecutive layers $MT_2 = (t_1 + t_3)/2 + t_2$. The distribution has the expected Gaussian shape, due to the intrinsic resolution, and a long tail at lower values due to the presence of parasitic tracks.

The two quantities MT_2 and MT_3, plotted one against the other in fig. 14, exhibit a strong correlation. The blob around the maximum drift time value is due to events not affected by parasitic track production. If only one drift time measurement is affected, the corresponding point lies along one of the four bands clearly visible in the picture, depending on the affected layer. The points cumulating along the $MT_2 = MT_3$ line are due to two simultaneous beam tracks crossing the detector.

A track measurement is considered affected by a parasitic track if one of the variables MT_2 and MT_3 is more than 2.5 standard deviations from the mean value of the Gaussian

fit to the distribution of fig. 13b. With this definition, the different contributions were computed, and the results are displayed in table 1.

Most of the extra tracks accompanying the muons are soft δ-rays which remain contained inside a cell. Therefore they affect only a single drift time measurement and do not give any trigger inefficiency.

The results given in table 1 indicate that about 20% of the muons produce extra tracks, and that for only 3.8% of the tracks two or more layers are affected.

A detailed study of this component shows that 0.8% can be ascribed to a pair of beam tracks crossing the detector, so the trigger inefficiency due to electromagnetic secondaries accompanying the muon is 3.0%. Furthermore about 50% of this last sample has only two drift time measurements affected, still providing useful information for the track reconstruction.

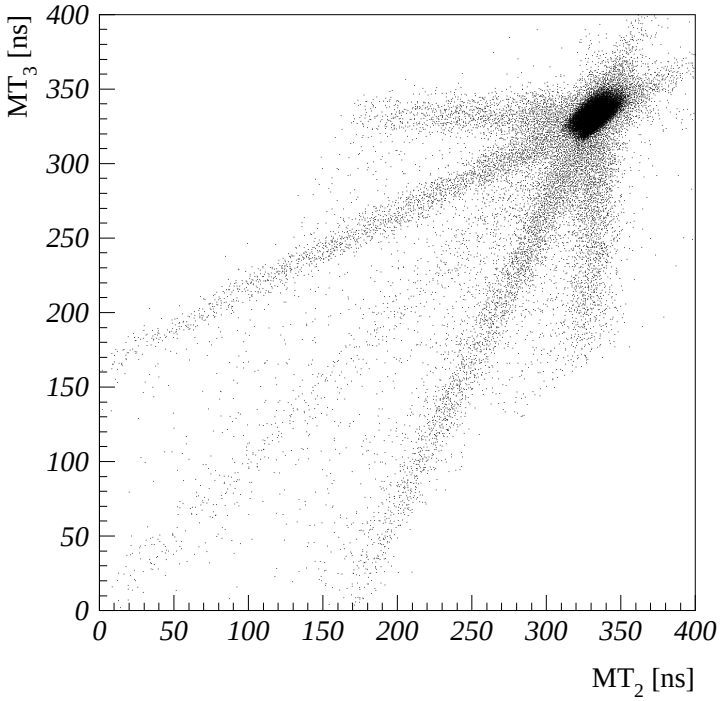

Figure 14: MT_2 *versus* MT_3

Table 1: *Parasitic tracks effect as percentage of tracks with various number of drift time measurements affected.*

No measurements affected		80.8 %
Only Layer 1 affected	3.4 %	
Only Layer 2 affected	3.6 %	
Only Layer 3 affected	4.1 %	
Only Layer 4 affected	4.3 %	
Single measurement affected		15.4 %
Double Beam Tracks	0.8 %	
Two Layers affected	1.5 %	
More than two Layers affected	1.5 %	
Two or more measurements affected		3.8 %

7 Drift Velocity

The average drift velocity, or conversely the maximum drift time (t^{max}), in a cell was obtained by fitting the position of the hits in the four layers to a straight line with the drift velocity as a free parameter. For this study only events with at least one hit per layer were used. The fit was repeated for all possible left-right combinations, and in case of multiple hits in a layer, for all possible hit combinations. Only the combination giving the smallest value of χ^2 was retained.

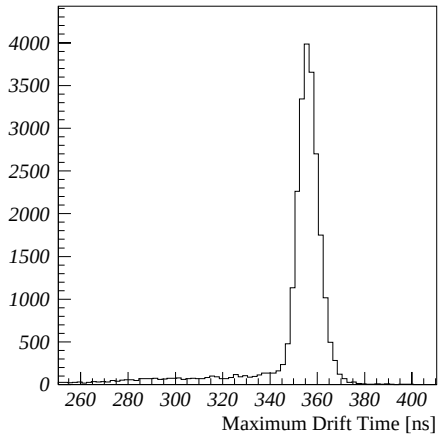

Figure 15: *Distribution of the maximum drift time.*

As an example, fig. 15 shows the distribution of the maximum drift time calculated event by event for a typical data set taken with the muon beam orthogonally incident.
The same quantity t^{max} can be calculated from the mean time of three consecutive layers, as described in section 6. The two methods give consistent results, as can be seen by comparing the distribution given in fig. 15 with the one displayed in fig. 13b. The linear fit method has the important advantage that it resolves automatically the left-right ambiguity in each cell, simplifying the analysis for large incidence angles.

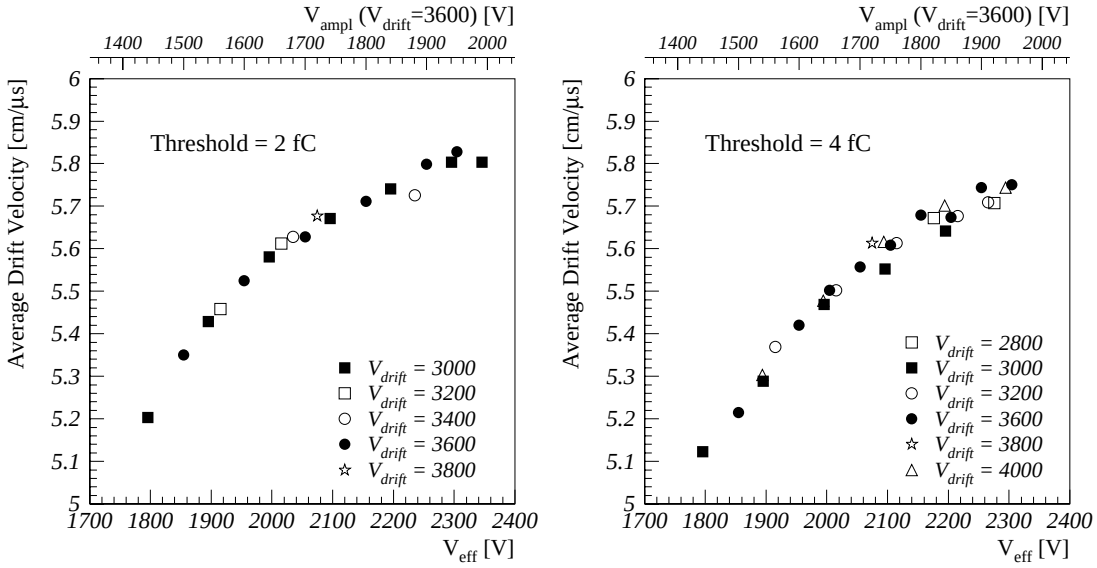

Figure 16: *Average drift velocities measured at different voltage and discriminator threshold settings. The measurements are plotted as a function of the effective voltage* V_{eff}*, proportional to the electric field on the wire.*

The drift velocity averaged along the total drift length is obtained from the relation $v_{\rm drift} = t^{max}/d$ where d is the wires pitch. Fig. 16 shows the results from the t^{max} distributions measured with data taken at various voltage and threshold settings.

For a given threshold value the average drift velocities measured for different voltage settings lie on the same curve, when plotted as a function of the effective voltage V_{eff}, defined in eq. 2. The dependence only on the electric field values in the immediate vicinities of the wire, confirms that the drift velocity is saturated for the wide range of voltage settings taken into account.

The dependence of the maximum drift time t^{max} on the threshold values and on V_{eff}, and thus on the gas amplification (see eq. 1), indicates that the first drifting electron is not sufficient for the signal detection. This effect must vanish at high amplification values, however a plateau is not to be expected because of the effective dependence of the drift velocity on the high electric fields close to the wire.

The variation of the apparent drift velocity as a function of the incidence angle of the tracks was studied by taking data with the chamber rotated around an axis orthogonal to the wires (longitudinal angle) and an axis parallel to the wires (transverse angle). The results, shown in fig. 17, confirm the naive expectation that the average drift velocity should be independent of the longitudinal angle and it should increase with the transverse angle reflecting the decrease in drift length.

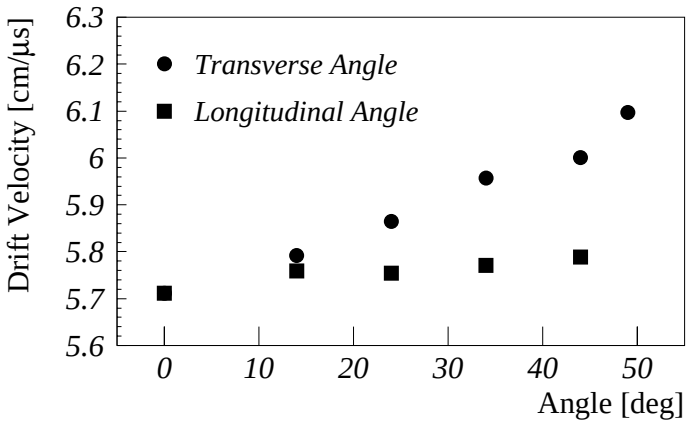

Figure 17: *Apparent drift velocities measured for different orthogonal and longitudinal incidence angles.*

The dependence of the apparent drift velocity on the incidence angle can be corrected at the track measurement stage, but it can generate systematic effects on the trigger efficiency, since the trigger algorithm expects the hits alignment to occur after the fixed delay t^{max} from the bunch crossing. A preliminary study on this subject has been reported in [8].

8 Linearity

One of the most important requirements on the chamber performance is a linear space-time relationship along the full drift space as needed by the Mean Timer method at the trigger level.

The linearity of the space-time relation was verified with the following formula :

$$\int_0^\tau \frac{1}{\rho(t)} \times \frac{\mathrm{d}N}{\mathrm{d}t}\,\mathrm{d}t \;=\; x(\tau) \;-\; x(0)$$

where $\rho(t)$ is the density function of the incoming tracks which can be extracted from the beam profile (fig. 18a) and $\mathrm{d}N/\mathrm{d}t$ is the drift time distribution in a cell (fig. 18b).

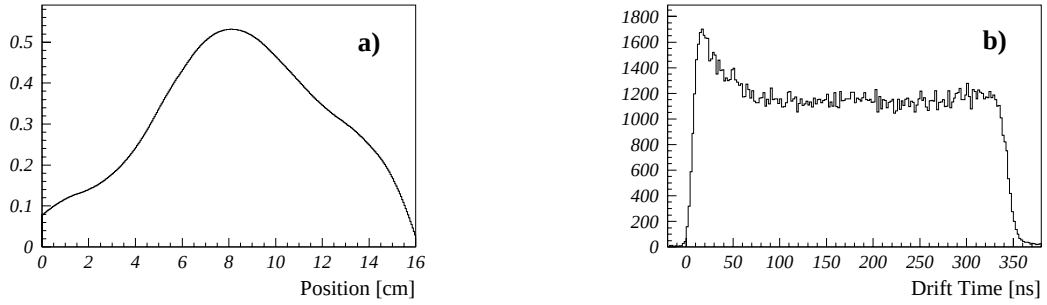

Figure 18: a) *Beam profile distribution.* b) *Typical Drift Time distribution of a cell.*

For this study a clean sample of orthogonally incident tracks with four hits was selected. The integral of the drift time distribution was calculated for each half-cell, weighting each entry according to the beam profile with the function $\rho(t)$. Each distribution was then fit to a straight line, and the deviation from linearity was calculated at each point and converted to a length, assuming a constant drift velocity.

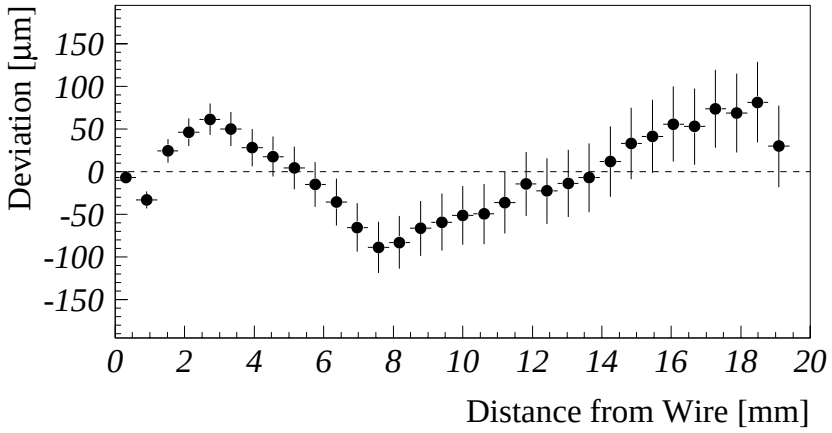

Figure 19: *Deviations from linear space-time relationship.*

Fig. 19 shows the deviation from linearity as a function of the distance from the wire along the half-cell, averaged among the half-cells illuminated by the beam. The non-linearity is everywhere within 100 μm, well below the intrinsic cell resolution.

9 Resolution

The widths of the Gaussian fits to the distributions of the MT_j variables, defined in equation 3 in section 6, were used to evaluate the intrinsic single cell resolution for different working conditions.

The resulting average cell resolution, measured at several amplification voltages and discriminator threshold settings with orthogonally incident tracks, is shown in fig. 20. The values at the plateau are well within the specifications required for the single cell resolution and guarantees some safety margin for the overall track resolution.

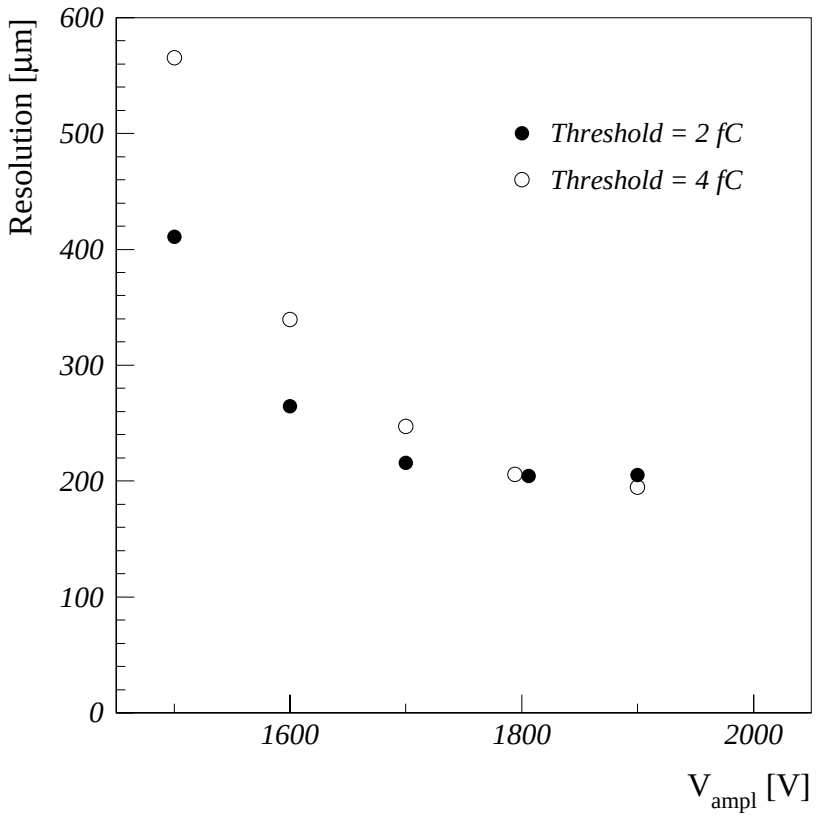

Figure 20: *Single point resolution evaluated at different voltages settings for orthogonally incident tracks.*

A more refined method was used to evaluate the dependence of the resolution on track incidence angle and position in the cell. The linear fit method already described in section 7 was used to select the 4 hits associated to a track and to resolve the left-right ambiguities. A linear fit was then applied to 3 out of the 4 drift time measurements associated to a track and the resolution was calculated from the residual of the discarded point, with the proper correction factors, for each of the 1 mm bins of the track position inside the cell. No corrections for non-linearities in the space-time relation were applied.

The resulting average resolutions are shown in fig. 21. The values are uniform and within the specifications along the full drift space for a wide range of transverse incidence angles, while a substantial deterioration can be observed for very large impact angles.

The influence of the transverse angle of incidence on the cell resolution is summarised in fig. 22. The *Global* values (open circles) represent the cell resolution obtained from the residuals of the track fits, integrated along the full drift space. The *Average*

values (full circles) are obtained as the average along the track positions of the resolutions of fig. 21.

The difference between the two values is due to the apparent non-linearity originated from the drift lines with the shortest path intercepted by the tracks with a transverse angle of incidence.

In order to study the improvement on the cell performance by the addition of the central electrodes the Aachen prototype had half of the drift cells without this electrode. The comparison of the resolution obtained for the two drift cells with different discriminator threshold and orthogonally incident tracks is shown in fig. 23. In all cases the resolution is considerably improved by the addition of the central electrodes.

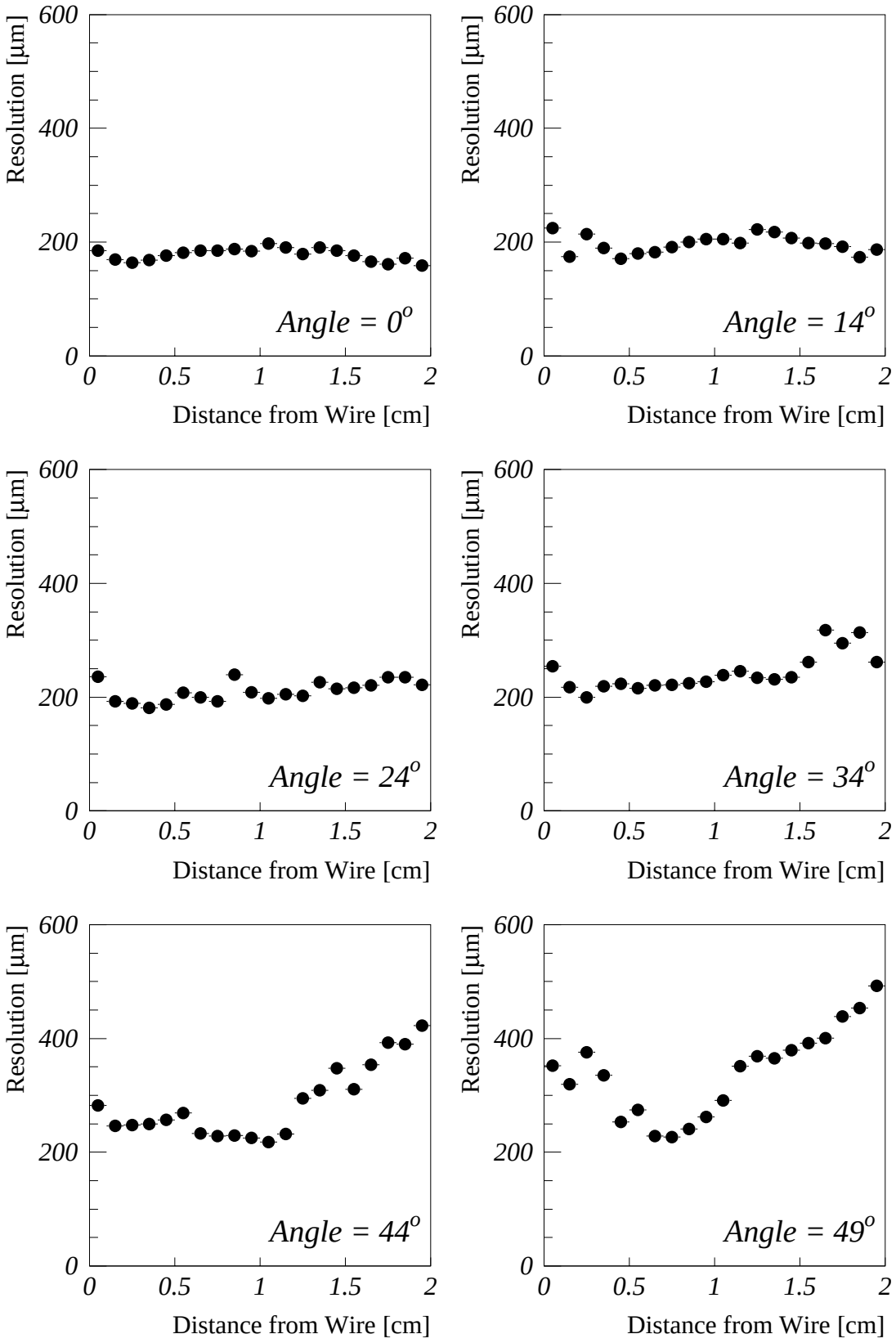

Figure 21: *Single point resolution calculated from the residuals of a track fit at different positions along the cell and for different incidence angles.*

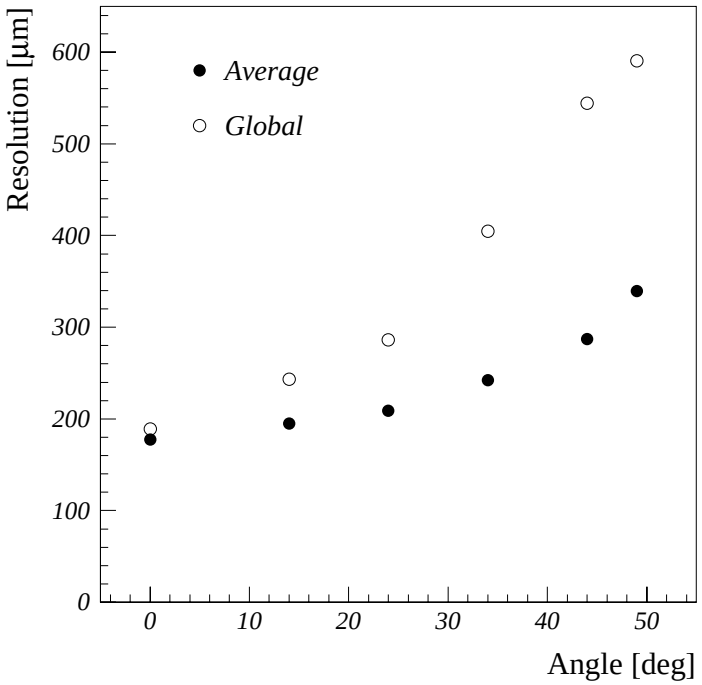

Figure 22: *Resolution for different incidence angles. Total cell resolution integrated along the full drift space (open circles). Resolution averaged along the track positions, from fig. 21 (full circles).*

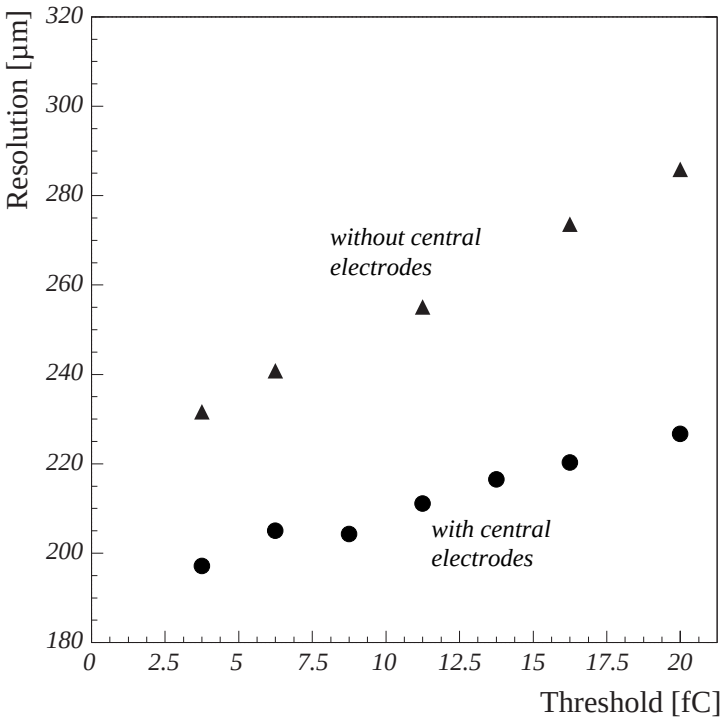

Figure 23: *Single point resolution for drift cells with and without central electrodes and different discriminator thresholds. The muon tracks are at normal incidence.*

10 Conclusions

The performance of the three drift tube chamber prototypes fully meets the required specifications for the barrel muon detector of the CMS experiment at LHC.

The cell design, with the addition of the supplementary electrodes, reaches a suitable efficiency and resolution for the track measurement. The linear space-time relation exhibited by the cell and the chosen structure of four layers of staggered cells, allows the first level triggering on the muon tracks, i.e. the bunch crossing and track parameters identification, by exploiting the correlation of signals in the four layers.

It is a remarkable result that the three prototypes, built in three different laboratories, and equipped with three different electronics, reach the same performance. This achievement make us confident that the chosen construction material and procedure lead to the uniformity necessary for a large scale production.

References

[1] CMS Technical Proposal, CERN/LHCC 94-38, LHCC/P1, 15 December 1994.

[2] F. Gasparini et al., Nucl. Instr. and Meth. A 336 (1993) 91.

[3] G. Barichello et al., Nucl. Instr. and Meth. A 360 (1995) 507.

[4] R. Veenhof, *GARFIELD, a Drift Chamber Simulation Program User's Guide*, Version 5.13, CERN Program Library W5050, 1995.

[5] F.M. Newcomer et al., IEEE Trans. on Nucl. Sci., 40 (1993) 630.

[6] P. Rewiersma, The L3 Wire Amplifier NH19-6112, NIKHEF 1986.

[7] E. Conti et al., *Experimental tests of the Q2 drift tubes prototype chamber for the CMS Muon Barrel*, CMS Note 1997/019.

[8] M. De Giorgi et al., Proceedings of the *First Workshop on Electronics for LHC Experiments*, CERN/LHCC 95-56, p.222.